RSC Advances

PAPER

View Article Online
View Journal | View Issue

Cite this: *RSC Adv.*, 2025, **15**, 45665

Anodic NiO nanoparticles as high-performance asymmetric supercapacitor devices in hybrid electrolytes

Muhammad Danish,†[a] Jawad Ahmad,†[af] Peer Muhammad,[b] Sofia Javed,[b] Anwar Saeed,[a] Nilem Khaliq,[c] Muhammad Haseem Bhatti,[a] Rizwana Ghazi,[d] Asna Fatima Kiyani,[e] Habib Ullah,[f] Yi Xie,[f] Imran Shakir*[g] and Ghafar Ali*[a]

The energy storage capabilities of a supercapacitor are critically determined by the choice of electrode materials, electrolytes, and synthesis methods, making their appropriate selection indispensable for improving the electrochemical performance. This study presents the synthesis of nickel oxide (NiO) nanoparticles (NPs) by a low-cost, straightforward, and one-step anodization approach. FESEM, HRTEM, XRD, XPS, BET analysis, FTIR, and Raman spectroscopy were performed to determine the morphology, crystal structure, oxidation states, specific surface area, functional groups, and vibrational and rotational states of NiO NPs. The fabricated electrode was investigated for capacitive application in 1 M KOH, Na_2SO_4 and hybrid electrolytes. The electrode showed an enhanced capacitance of 1748 F g^{-1} at 2.0 A g^{-1} in the hybrid electrolyte compared to 1116 F g^{-1} in KOH and 816 F g^{-1} in Na_2SO_4. The fabricated asymmetric supercapacitor device (NiO//AC) achieved a specific capacitance of 172 F g^{-1} at 2 A g^{-1} with an energy density of 34.4 Wh kg^{-1} at a power density of 900 W kg^{-1}. Notably, the device retained 94% capacitance after 8000 cycles at 5 A g^{-1}. The improved performance can be attributed to the high surface area of NiO NPs, enhanced conductivity, and improved charge kinetics in the hybrid electrolyte. This result demonstrates the potential of anodic NiO NPs as efficient materials in hybrid electrolytes for supercapacitor applications.

Received 16th September 2025
Accepted 6th November 2025

DOI: 10.1039/d5ra07019h

rsc.li/rsc-advances

1 Introduction

The energy storage devices, especially supercapacitors (SCs), have attracted a lot of attention due to the increasing demand for efficient, sustainable, and high-power energy storage devices. SCs have several important features including high power density, rapid charge–discharge capability, and high cycling stability.[1,2] The SCs are classified into electric double-layer capacitors and pseudocapacitors based on the charge storage mechanism. The electrode stores charges on the surface in electric double layers using carbon-based materials such as graphite, graphene, and CNTs, while the pseudocapacitor stores charges faradaically *via* redox reactions on the surface as well as at the electrode interface by transition metal oxides.[3] Although they show great promise, the SCs suffer from major challenges such as limited energy density and high self-discharge rate, which hamper their practical applications. Lithium-ion batteries (LiBs) usually exhibit high energy density but lower power density in comparison with SCs. To bridge the gap between these two technologies, most of the researchers focus to develop innovative strategies to overcome these limitations. In this regard, effective design of electrode materials and selection of electrolytes play a vital role for better energy and power densities of SCs.

The selection of the electrode material is decisive for defining the capacitance, conductivity, and stability of SCs by providing multiple active sites for charge storage. Similarly, the selection of electrolytes influences the ionic transport and voltage window, which has great impact on the performance of the SCs. These factors necessitate cost-effective, scalable electrode materials, and suitable electrolyte selection for the optimal SC performance.[4] Most of the reports show that carbon-based electric double-layer capacitors have limited energy density and specific capacitance which is replaced by transition metal oxides (TMOs) having high energy density and stability.[5,6] To date, various TMOs including V_2O_5, MnO_2, TiO_2, NiO, and

[a]*Nanomaterials Research Group, Physics Division, PINSTECH, Islamabad 45650, Pakistan. E-mail: ghafarali@kaist.ac.kr*

[b]*School of Chemical and Materials Engineering (SCME), National University of Science and Technology (NUST) Islamabad, Pakistan*

[c]*Department of Physics, Women University Swabi, KPK, Pakistan*

[d]*Department of Chemistry, Quaid-i-Azam University, Islamabad 45320, Pakistan*

[e]*School of Chemistry, University of Edinburgh, Scotland, UK*

[f]*State Key Laboratory of Silicate Materials for Architectures, Wuhan University of Technology, No. 122, Luoshi Road, Wuhan 430070, China*

[g]*Department of Physics, Faculty of Science, Islamic University of Madinah, Madinah 42351, Saudi Arabia. E-mail: imranskku@gmail.com*

† Both authors have equal contributions.

CuO have been explored as electrode materials for high-performance supercapacitor applications.[1,7–10] Compared to other TMOs, nickel oxide (NiO) has shown promising performance as a SC because of high theoretical capacitance (~2584 F g^{-1}),[11] low cost, environmental sustainability, and multiple oxidation states conducive to fast redox reactions.[12] These characteristics allow efficient charge storage through reversible faradaic redox reaction at the interface and robust structural stability, making it a potential option for charge storage application.[13,14] Effective utilization of the abovementioned properties required suitable synthesis procedures that precisely control the morphology and surface characteristics of NiO NPs. Different techniques have been described for the synthesis of NiO NPs including hydrothermal,[15] chemical capping,[16] and sol gel methods.[17] However, these methods have high risks of impurity incorporation besides complex processing, high temperature, and limited morphology control. Anodization has emerged as a simple approach to produce NiO NPs, allowing precise control of particle size, porosity, and surface area. These parameters are essential for improving the electrochemical performance in supercapacitor application.[18]

Complementing the role of NiO NPs, the choice of electrolyte significantly affects the electrochemical performance of SCs by modulating the ionic transport dynamics and accessible potential range. To evaluate the influence of diverse electrolytes on the performance of SCs based on anodic NiO NPs, we used three types of electrolytes: potassium hydroxide (KOH), sodium sulfate (Na_2SO_4), and their combination to form a hybrid electrolyte. We found that the hybrid electrolyte demonstrated superior performance compared to the two electrolytes, which is attributed to the synergistic impact that improves ionic mobility and electrochemical activity at the electrode–electrolyte interface.

This study presents a novel approach for the synthesis of NiO NPs *via* green, simple and cost-effective, one-step anodization method. We systematically explore the influence of various electrolytic solutions (KOH, Na_2SO_4, and hybrid) on the performance of NiO NP-based SCs. The results demonstrate that the NiO electrode showed an improved specific capacitance of 1748 F g^{-1} in the hybrid electrolyte. Moreover, the fabricated asymmetric SCs device showed a fascinating electrochemical performance with an enhanced energy density of 34.4 Wh kg^{-1}. The results highlight the synergistic role of NiO NPs in the hybrid electrolyte for the advancement of future high-performance energy storage supercapacitors.

2 Experimental procedure

2.1. Materials and chemicals

A nickel (Ni) sheet (0.1 mm thickness, 99.99% purity) was acquired from Goodfellow England, UK. Reagent-grade sodium chloride (NaCl, 99.99% purity), potassium hydroxide (KOH, 99.99% purity), sodium sulfate (Na_2SO_4, 99.99% purity), and sulfuric acid (H_2SO_4, 98%) were acquired from Merck, Germany. Ethanol and acetone were all analytical reagents purchased from Sigma Aldrich, USA. Ni foam and Al foils were also obtained from Goodfellow, England, UK. Deionized (DI) water was used as the electrolyte.

2.2. Anodization of Ni sheets

Prior to anodization, Ni sheets were cleaned by sonicating in ethanol and acetone for 5 min each, followed by rinsing with DI water, and drying in an oven at 60 °C. The anodization process was carried out in a homemade two-electrode setup, where a platinum plate ($15 \times 25 \times 0.2$ mm^3) served as the cathode and a Ni sheet as the anode, as shown in the schematic (Fig. S1). Anodization was conducted at a fix voltage (10 V) in a 1 M NaCl aqueous electrolyte at room temperature using a DC power supply (Tektronix PWS 4305, USA). When the power supply was switched on, the electrolytic solution turned light greenish as the Ni sheet (anode) starts to dissolve to form oxide precipitates, accompanied by significant hydrogen gas (H_2) evolution on the cathode surface. Over anodizing time (20–30 minutes), the entire Ni sheet was converted into solid-oxide precipitates, which are settled down at the bottom of the beaker. The precipitates were then dispersed and sonicated in DI water for 5 min using an ultrasonic bath (Elma E60H, Germany), and then collected using a centrifuge machine to remove the impurities if incorporated into the material. This cyclic process was repeated several times to ensure the complete removal of the salt. The precipitates were then dried overnight in an oven at 70 °C, ground into powder, and collected. The resulting powder was annealed at 450 °C for 2 h and then cooled down at natural room temperature.

The specific anodic and cathodic reaction for the anodization of the Ni sheet is as follows:

At the anode:

$$Ni \rightarrow Ni^{2+} + 2e^-$$

The produced Ni^{2+} ions react with hydroxide ions formed in the electrolyte to produce nickel hydroxide.

$$Ni^{2+} + 2OH^- \rightarrow Ni(OH)_2$$

The annealing process transformed $Ni(OH)_2$ into NiO *via* the following reaction:

$$Ni(OH)_2 \rightarrow NiO + 2H_2O$$

At the cathode:

The evolution of hydrogen gas (H_2) occurs at the cathode.

$$2H_2O + 2e^- \rightarrow H_2 + 2OH^-$$

The overall anodic and cathodic reaction is given as follows:

$$Ni + 2H_2O \rightarrow Ni(OH)_2 + H_2$$

2.3. Preparation of electrodes

Initially, a Ni foam was activated by sonication in 6 M H_2SO_4 for 30 minutes, followed by sonication in ethanol and DI water for 15 minutes each. Then, active materials (NiO NPs and $Ni(OH)_2$ nanoflowers used separately along with carbon black and poly(vinylidenefluoride-hexafluoropropylene) (PVDF-HFP) used as a binder) were combined in a percentage ratio of 70 : 20 : 10, and an appropriate amount of *N*-methylpyrrolidone (NMP) that serves as a solvent was added. The mixture was stirred for 24 hours (h) to form a uniform and homogeneous slurry. The slurry (~1.0 mg) was then pasted onto a Ni foam (with an active area of ~0.5 cm^2) and dried in a vacuum oven at 60 °C for 24 h. Fig. S2 shows the schematic diagram of the whole process from the synthesis of NiO NPs to the electrochemical properties measurements.

2.4. Fabrication of the NiO//Activated carbon asymmetric supercapacitor device

For the asymmetric SC device fabrication, NiO NPs was coated over one piece of Ni foam and activated carbon (containing 75 wt% activated carbon and 25 wt% PVDF-HFP) on another piece of Ni foam, which served as an anode and cathode, respectively. Whatman filter paper and hybrid electrolyte (1 : 1, KOH : Na_2SO_4) were used as separator and conduction media, respectively, between these electrodes for the SC device. The size of the synthesized device was (1 × 1) cm^2, which was applied to glow the commercial LEDs.

2.5. Characterizations

The crystal structure and phase purity of the prepared samples were studied using an XRD (Rigaku, 2500 V diffractor, Japan) with Cu Kα radiation (λ = 1.5418 Å) at 40 kV. The surface morphology of the prepared materials was investigated using an FESEM (UHR-SEM Magellan 400, FEI, USA) and a HRTEM (Techni G2 F30, FEI, USA). The composition of samples was determined using an energy-dispersive X-ray (EDX) spectrometer equipped with an FESEM. The selected area electron diffraction (SAED) patterns were obtained using a TEM. Surface area was measured by the Brunauer–Emmett–Teller (BET) method, and the pore size distribution was determined by the Barrett–Joyner–Halenda (BJH) method. Fourier-transform infrared (FTIR) spectroscopy was performed using a Nicolet iS50 FTIR spectrometer in the range of 4000–400 cm^{-1}. Raman spectra were recorded using a high-resolution dispersive Raman spectrometer (Lab RAM HR, Horiba Jobin Yvon, France). A He–Ne laser producing 514 nm was used as the excitation source for the Raman spectrometry. X-ray photoelectron spectroscopy (XPS) analysis was carried out using a spectrometer (Sigma Probe, Thermo VG Scientific) with an Al Kα excitation source operating at 15 kV and 7 mA. The binding energies were calibrated using the C 1s peak (~285.5 eV).

2.6. Electrochemical measurements

The cyclic voltammetry (CV), galvanostatic charge–discharge (GCD), and electrochemical impedance spectroscopy (EIS) were performed using an electrochemical workstation (Biologic, VSP-300, France) in aqueous electrolytes of 1 M KOH, 1 M Na_2SO_4, and 1 M hybrid. A three-electrode system was used where the prepared material coated on a Ni foam serves as the working electrode, a platinum electrode as the cathode, and a $Hg/HgCl_2$ electrode as the reference electrode. The CV measurements were carried out at different scan rates (10 to 60 mV s^{-1}) with voltage window of −0.2 to 0.8 V. The GCD measurements were performed at current density in the range of 2–5 A g^{-1} with voltage window of 0 to 0.5 V. The EIS measurements were conducted in the frequency range of 0.1 Hz to 100 kHz. All the electrochemical measurements were recorded at room temperature. The CV and GCD of the SC device were performed in the potential window of 0 to 1.2 V in the 1 M hybrid electrolyte using a two-electrode system. The EIS measurement of the fabricated SC device was conducted in the frequency range of 0.1 Hz to 140 kHz.

Furthermore, the specific capacitance (C_s), energy density (E), and power density (P) of the assembled asymmetric supercapacitor device were calculated using eqn (1)–(3):

$$C_s = \frac{I \times \Delta t}{m \times \Delta V} \quad (1)$$

$$E = \frac{C_s \times \Delta V^2}{7.2} \quad (2)$$

$$P = \frac{3600E}{\Delta t} \quad (3)$$

where "ΔV" and "t" are the discharge voltage and discharge time of the fabricated device, respectively.

3 Results and discussion

3.1. Structural, morphological and compositional analyses

The structural and phase-related properties of the prepared samples were investigated by XRD, as shown in Fig. 1. For the as-prepared sample, *i.e.*, $Ni(OH)_2$, the peaks observed at ~19.2°, 33°, 38.5°, 39°, 52.1°, 59°, 62.7°, 69.3°, and 72.7° can be

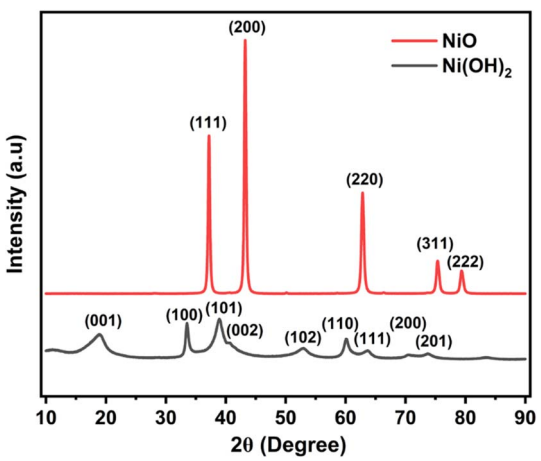

Fig. 1 XRD pattern of the $Ni(OH)_2$ nanoflowers and NiO NPs prepared *via* anodization in 1 M aqueous NaCl electrolyte.

assigned to the (001), (100), (101), (002), (102), (110), (111), (200), and (201) planes of hexagonal phase of $Ni(OH)_2$, respectively (ICDD card # 14-0117). This result shows that $Ni(OH)_2$ produced *via* anodization have adequate crystallinity even without thermal treatment. This fact has also been observed when various anodic metal-oxide NPs showed good crystallinity in the their as-anodized forms as reported in our previous article.[18] However, crystallinity after annealing in air for 2 h at 450 °C of the NiO NPs has increased tremendously with the emergence of new diffraction peaks located at ~37.2°, 43.2°, 62.8°, 75.4°, and 79.4° correspond to the (111), (200), (220), (311), and (222) planes of the cubic NiO respectively (ICDD card # 47-1049). It is known that $Ni(OH)_2$ is an intermediate phase and transforms into a stable phase of NiO, when calcined at a temperature range of 400–600 °C.[19] We found that calcination at 450 °C for 2 h results in the transformation of hexagonal $Ni(OH)_2$ nanoflowers into the cubic phase of NiO NPs (ICDD card # 47-1049), as given in the XRD patterns of the annealed sample.[19] No extra peak was found in the diffraction pattern, which confirms the high purity of NiO NPs produced *via* the anodization process.

The morphological study of the as-anodized and annealed samples was explored by FESEM and HRTEM along with EDX analysis. Fig. 2a depicts the FESEM image of $Ni(OH)_2$ revealing the formation of nanoflower-like morphology obtained as a result of Ni sheet anodization in 1 M NaCl electrolyte at room temperature. This type of morphology is reported on the surface of Fe-sheet when anodization was carried out in an ethylene glycol-based electrolyte.[20] The low-magnification image (Fig. 2a) exhibits the formation of a nanostructure comprising small nanoflowers, which agglomerate in such a way that it generated a large flower. This can be attributed to the continuous formation of small nanoflowers, which combined together to generate large flowers due to temperature increase observed during anodization. The diameter of the nanoflowers is in the range of ~2–6 μm. The high-magnification image of the single nanoflower is shown in Fig. 2b. These nanoflowers are not well interconnected to eachother like reported in our articles.[20,21] Previously, we have produced nanoflower- and hierarchical nanosheet-like morphologies in the form of thin film as a result of Fe and Mg sheet anodization in ethylene glycol-based electrolytes, respectively. While in the present case, the anode (Ni sheet) is dissolved completely in 1 M NaCl electrolyte with anodization time contrary to Fe and Mg anodes (sheets), which remained stable during anodization in an ethylene glycol-based electrolyte. The EDX spectrum of nickel hydroxide nanoflowers (Fig. 2c) exhibits Ni and O peaks along with a very small peak of Cl incorporated from the electrolyte solution. Fig. 2d shows the low-resolution TEM image of the as-prepared sample, which also confirms the origin of $Ni(OH)_2$ nanoflowers, thus further verifying the FESEM results. The single nanoflower was depicted in the high-resolution TEM image of $Ni(OH)_2$ in Fig. 2d. A large amount of crystallites can be observed throughout the sheet, corroborating the XRD results.

Interestingly, the FESEM image of the annealed sample at low magnifications (Fig. 3a) reveals the formation of NPs, which can be ascribed to the calcination process at 450 °C for 2 h in air. It is important to mention that the annealing process completely changed the morphology from nanoflowers into

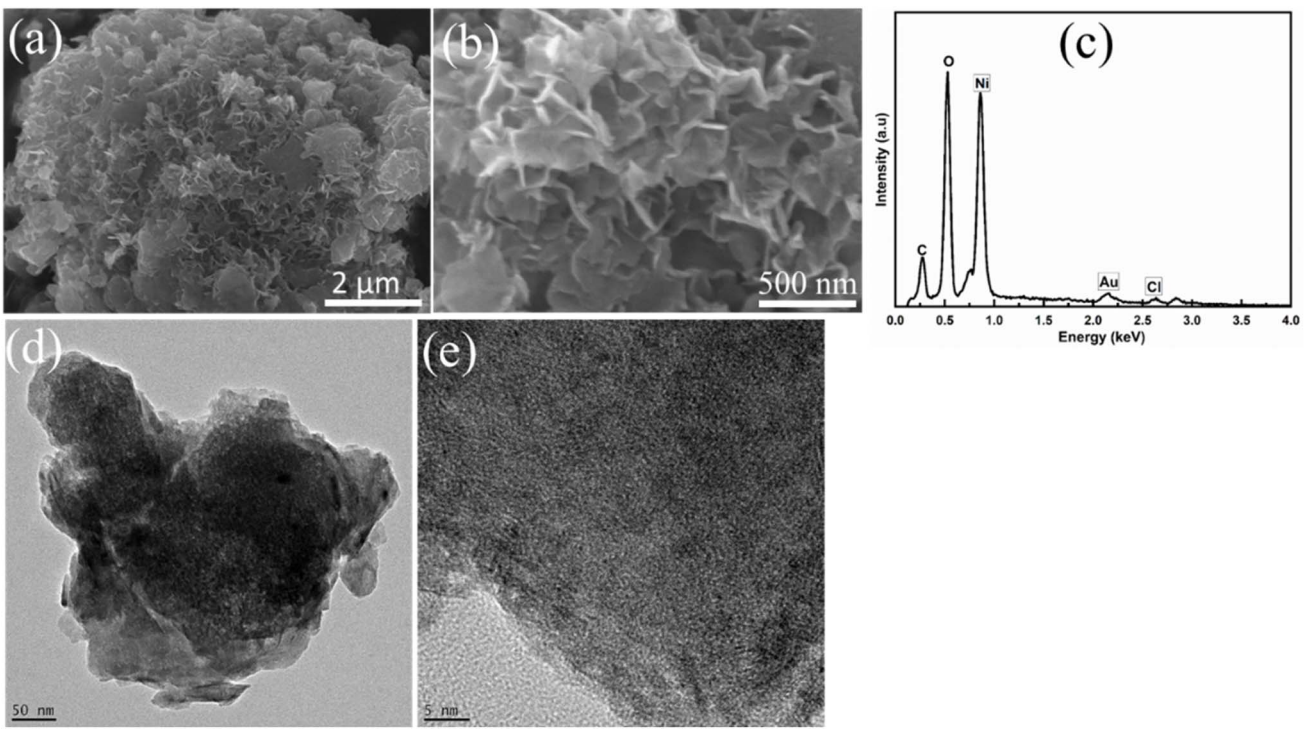

Fig. 2 (a) FESEM image of the as-prepared anodic $Ni(OH)_2$ showing the formation of nanoflowers, (b) high-magnification image of a single nanoflower, (c) EDX spectrum showing the composition of $Ni(OH)_2$ nanoflowers, (d) low-resolution TEM image, and (e) HRTEM image of the $Ni(OH)_2$ nanoflowers.

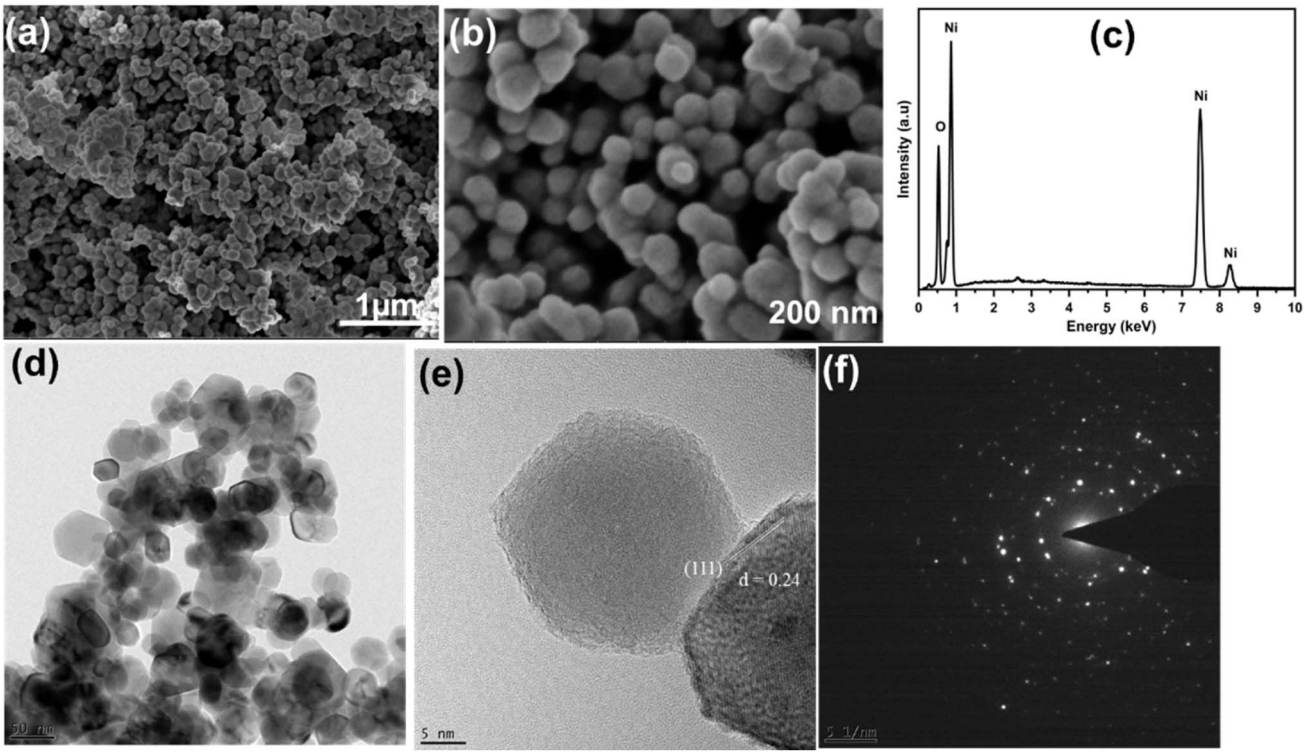

Fig. 3 (a) FESEM images of the annealed anodic NiO, showing the formation of NPs, (b) high-magnification image, (c) EDX spectrum of NiO NPs, (d) low-resolution TEM image of the NiO NPs, (e) HRTEM image of the NiO NPs, and (f) SAED pattern indicating the polycrystalline nature of the anodic NiO NPs.

spherical NPs. This kind of morphological change has been observed in our previous work on Fe-anodization.[20] These NPs are homogeneous with uniform diameters. The average size of the NP is around 20 nm, as can be seen in the high-magnification SEM image (Fig. 3b) without the formation of any agglomerates. The purity of the annealed NiO NPs has been confirmed from the EDX analysis (Fig. 3c), which shows the peak of Ni and O only without any impurity which is in good agreement with the XRD result. The small Cl peak in the EDX spectrum of $Ni(OH)_2$ is not detected after calcination, which is most probably evaporated as Cl_2.

It can be seen from the TEM image of NiO (Fig. 3d) that after annealing, the nanoflower morphology of $Ni(OH)_2$ is completely transformed into homogeneous and uniform NiO NPs. Moreover, the NPs are spherical in shape with clear boundaries and each particle can be identified and distinguished easily. Fig. 2e displays the HRTEM image of NiO NPs with a fringe of 0.24 nm corresponding to the (111) plane of NiO and in good agreement with the XRD result. The morphological evolution from nanoflowers arrangement of $Ni(OH)_2$ to the spherical NiO NPs upon annealing is highly beneficial for electrochemical applications due to enhanced crystallinity and high surface area. The annealed NiO NPs offers a larger active surface area, which improves ionic diffusion, contributing to the enhanced charge storage capacity and cycling stability in supercapacitor devices.

The surface area of the synthesized $Ni(OH)_2$ nanoflowers and NiO nanoparticles were assessed through nitrogen adsorption–desorption analysis performed at 77 K. Fig. 4a and b illustrates that the isotherm corresponds to the type IV adsorption curve for NiO and $Ni(OH)_2$, featuring a distinct hysteresis loop that indicates the mesoporous structure of NiO nanoparticles. The specific surface area of the NiO NPs, determined using the Brunauer–Emmett–Teller (BET) model, was calculated to be 38 $m^2\ g^{-1}$ in contrast to $Ni(OH)_2$, which measured 20 $m^2\ g^{-1}$. Furthermore, the Barrett–Joyner–Halenda (BJH) analysis of NiO NPs reveals an average pore diameter of approximately 4.5 nm in contrast to the 38 nm observed in $Ni(OH)_2$ nanoflowers, as illustrated in Fig. 4c. NiO NPs demonstrated a high surface area compared to $Ni(OH)_2$ nanoflowers. The high surface area can be related to the thermal transformation of $Ni(OH)_2$ nanoflowers into NiO NPs, which re-arranged the structure and removed the lattice bound water. The higher surface area coupled with enhanced crystallinity of NiO NPs can provide a rapid ionic transport and facilitate abundant active sites for redox reactions, which is beneficial for energy storage applications.[22,23]

The FTIR spectra of the as-prepared $Ni(OH)_2$ nanoflowers and annealed NiO NPs are shown in Fig. S3. The absorption bands of $Ni(OH)_2$ nanoflowers positioned at 450, 532, and 640 cm^{-1} correspond to Ni–O and Ni–OH bending and stretching vibrations within the layered structure of $Ni(OH)_2$.[24] While the bands at 1376 cm^{-1} and 1620 cm^{-1} originate from the bending vibrations of adsorbed carbonate and water, respectively, the bands at 3415 cm^{-1} and 3640 cm^{-1} are attributed to the stretching vibration of O–H and adsorbed water.[25] The weaker band at 2345 cm^{-1} results from the adsorption of CO_2 from atmosphere.[26] In contrast, the removal of hydroxyl groups

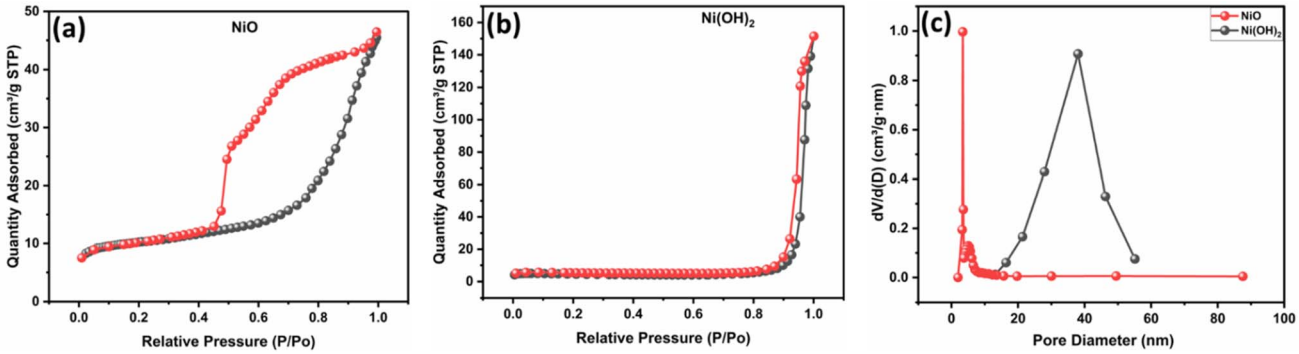

Fig. 4 N_2 adsorption–desorption isotherm of the (a) NiO NPs, (b) $Ni(OH)_2$ nanoflowers, and (c) distribution of the pore size behavior of both samples.

after annealing confirms the transformation of the $Ni(OH)_2$ phase into NiO NPs. Notably, at the same time, the emergence of a new band at 430 cm^{-1} and 485 cm^{-1} demonstrate the Ni–O stretching vibration in the cubic NiO structure.[27]

To examine the structural features and phase transformation from $Ni(OH)_2$ nanoflowers to NiO NPs, Raman spectroscopy was further employed, as shown in Fig. 5. In the case of $Ni(OH)_2$, the low-frequency peaks at 197 cm^{-1} and 373 cm^{-1} are related to the bending mode of the Ni–O bond and the stretching vibration of the O–H bond in $Ni(OH)_2$. The most intense peak at 560 cm^{-1} corresponds to the stretching vibrations of the Ni–OH bond, whereas the small band at 684 cm^{-1} may be related to overtone or combination modes associated with the layered hydroxide lattice.[28] The Raman peak at 1060 cm^{-1} in $Ni(OH)_2$ is primarily attributed to the symmetric stretching of Ni–O bonds within the $Ni(OH)_2$ structure. In contrast, after thermal treatment, the Raman spectrum of NiO shows the characteristic peaks of cubic NiO. The most prominent peak in the Raman spectrum appeared at 517 cm^{-1} corresponding to the first-order longitudinal optical (LO) phonon mode of nano-crystalline NiO.[29] A weaker peak for transverse optical (TO) at 382 cm^{-1} can be ascribed to the disorder-induced scattering commonly reported in the NiO nanostructure.[30] Furthermore, the peaks around 684 cm^{-1} and 1060 cm^{-1} are attributed to the combination of the second-order phonon mode involving 2TO and 2LO, respectively.[30,31] The disappearance of the intense Ni–OH stretching mode (~560 cm^{-1}) and other hydroxide-related peaks alongside the emergence of the new characteristic Ni–O lattice mode at ~517 cm^{-1} in NiO clearly confirmed the successful thermal decomposition of $Ni(OH)_2$ nanoflowers into NiO NPs. Therefore, Raman measurements further justify the XRD results. Additionally, the elemental composition and valence state of NiO NPs were investigated by X-ray photoelectron spectroscopy (XPS). The deconvoluted spectra of Ni 2p are shown in Fig. 6a, with two major noticeable peaks at 852.4 eV and 870 eV and a minor peak at about 860 eV that corresponds to Ni $2p_{3/2}$, Ni $2p_{1/2}$, and satellite peak of Ni 2p, respectively.[32] Moreover, the high-scan spectrum of oxygen (Fig. 6b) has a single main peak at ~532 eV, which is due to the Ni–O bond that is beneficial for capacitance improvement.[33]

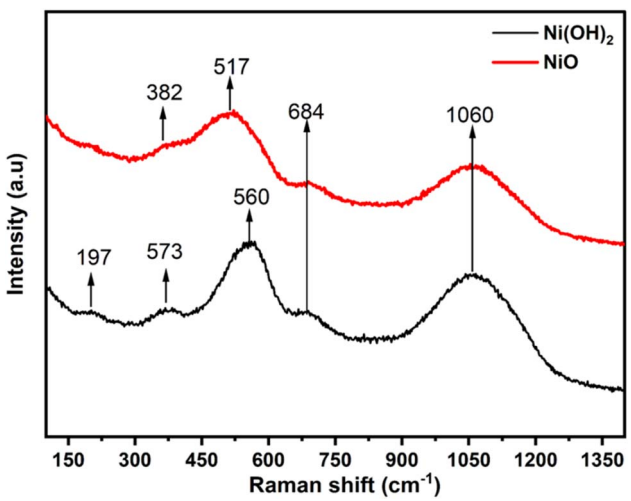

Fig. 5 Raman spectra of the $Ni(OH)_2$ nanoflowers and NiO NPs prepared *via* anodization in 1 M aqueous NaCl electrolyte.

3.2. Electrochemical behavior of the NiO electrode in KOH

The electrochemical performance of the NiO NP-based electrode was evaluated in the presence of 1 M KOH. Fig. 7a presents the CV response of the NiO electrode recorded at different scan rates from 10 to 60 mV s^{-1}. It exhibits a distinct redox peak which demonstrates a purely pseudocapacitor nature. The overall shape of the CV curves remains the same even at high scan rates, which shows the excellent stability and reversibility of the NiO electrode. Fig. 7b shows the GCD curves of the NiO electrode at different current densities ranging from 2 to 5 A g^{-1}. The corresponding values of specific capacitance calculated from the GCD curves at different current densities are presented in Fig. 7c. The maximum specific capacitance obtained in a KOH electrolyte is ~1116 F g^{-1} at 2 A g^{-1}. The redox mechanism responsible for charge storage at the NiO electrode arises from the following reactions:

$$NiO + OH^- \leftrightarrow NiOOH + e^- \quad (4)$$

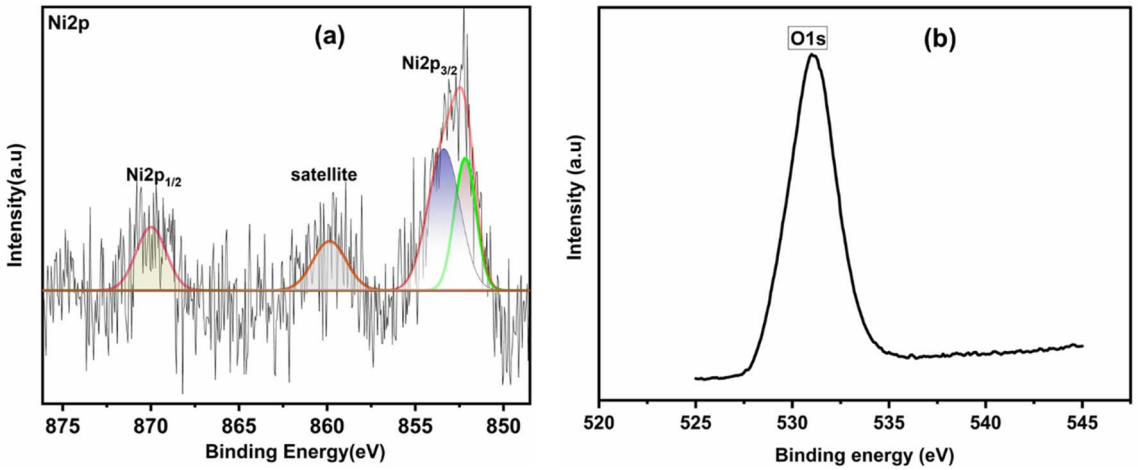

Fig. 6 High-scan XPS spectrum of (a) Ni 2p and (b) oxygen O 1s of the NiO NPs prepared *via* anodization in a 1 M aqueous NaCl electrolyte.

3.3. Electrochemical behavior of the NiO electrode in Na_2SO_4

The electrochemical behavior of the NiO electrode was also investigated in 1 M Na_2SO_4. Fig. 7d depicts the CV response of the NiO electrode under different voltage scans ranging from 10 to 60 mV s^{-1}. The figure indicates the absence of a strong redox peak in a neutral electrolyte, which can be attributed to Na^+ and SO^{4-} adsorbed on the surface of the electrode. In the neutral electrolyte such as Na_2SO_4, the high concentration of SO_4^{2-} ions with a large radius results in the surface faradaic reaction instead of intercalation, which usually occurred in OH^- with a relatively small radius. Therefore, the nearly rectangular shape with the absence of strong redox peaks in the CV is due to the surface dominant redox process.[4] It can be seen that even at a high scan potential, the CV curves remain unchanged, which reveals the stability of the NiO electrode. Fig. 7e represents the GCD curves of the NiO NP electrode at different current densities ranging from 2 to 5 A g^{-1}. The specific capacitance at different current densities was also calculated, and is shown in Fig. 7f. The maximum specific capacitance achieved in a Na_2SO_4 electrolyte is ~816 F g^{-1} at 2 A g^{-1}.

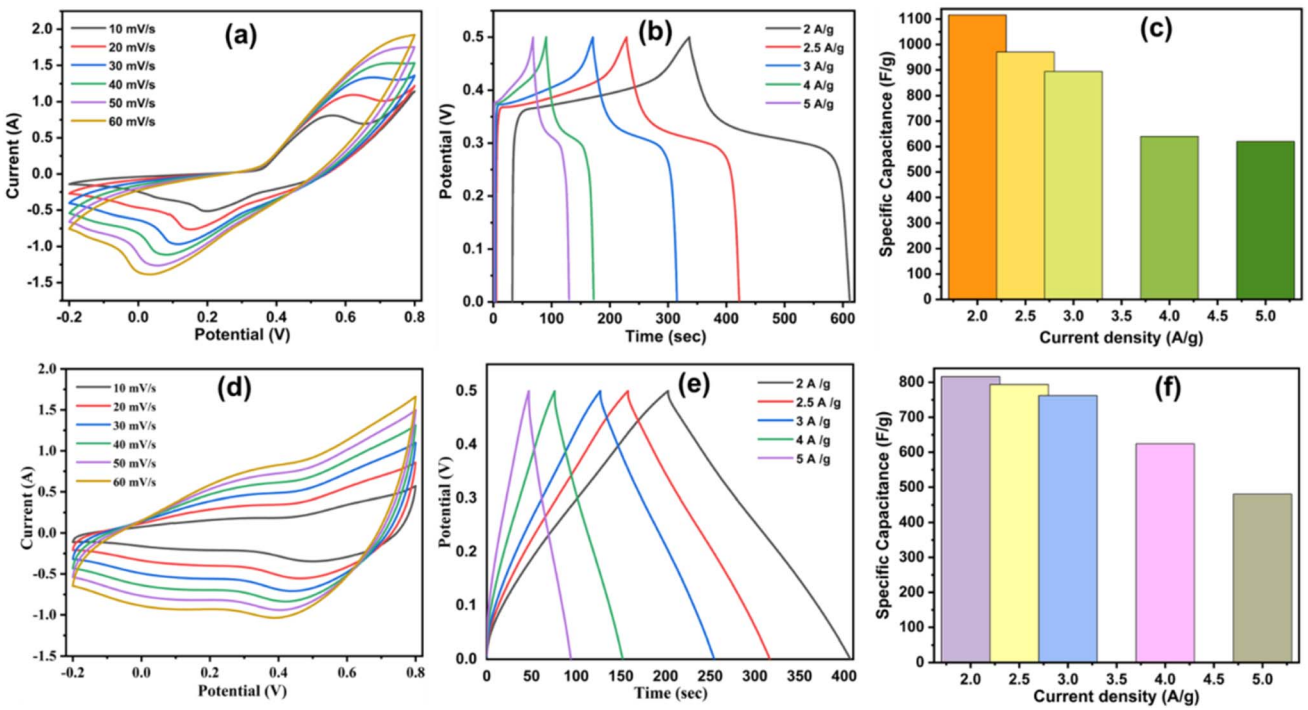

Fig. 7 Electrochemical performance of the NiO electrode in a 1 M KOH electrolyte: (a) CV response, (b) GCD curves and (c) specific capacitance at different current densities. Electrochemical performance of the NiO electrode in a 1 M Na_2SO_4 electrolyte, (d) CV response, (e) GCD behavior and (f) specific capacitance at different current densities.

3.4. Electrochemical performance of the NiO electrode in the hybrid electrolyte

Fig. 8 represents the electrochemical behavior of $Ni(OH)_2$ nanoflowers and NiO NP electrodes in the hybrid electrolyte (1 : 1 KOH and Na_2SO_4). Fig. 8a shows the CV response of the NiO NP electrode at different sweep rates from 10 to 60 mV s^{-1} in a voltage window of −0.2 to 0.8 V. The CV results reveal the pseudocapacitive behavior of the electrode. All CV curves have anodic and cathodic peaks that represent the reversible redox reactions of Ni^{2+} and Ni^{3+} in NiO.[34] The duck-like shape of the CV curves is maintained even at high sweep rates, demonstrating that the NiO NP electrode has outstanding rate performance and reversibility. Furthermore, the capacitive properties of the electrodes were determined by the GCD curves. Fig. 8b shows the comparison of the GCD curves of $Ni(OH)_2$ and NiO electrodes at 2 A g^{-1}. It can be seen that the NiO electrode has a longer discharge duration/charge retention than that of the $Ni(OH)_2$ electrode. Fig. 8c shows the GCD curves of NiO electrodes at different current densities (2–5 A g^{-1}). The specific capacitance calculated from the GCD curves at different current densities from 2 to 5 A g^{-1} was approximately 1748, 1540, 1506, 1486, and 1330 F g^{-1}, respectively. Moreover, the trend of energy density and specific capacitance of both the electrodes with respect to current density is given in Fig. 8d and e, respectively. The considerably higher capacitance performance and high energy density of NiO compared to the $Ni(OH)_2$ electrode can be attributed to its high surface area, enhanced crystallinity, and good electronic conductivity, which significantly improve the charge transfer kinetics. It is noted that our fabricated NiO electrode has an outstanding performance in comparison to the reported work, as given in Table 1. Additionally, for comparison, the electrochemical performance of the $Ni(OH)_2$ electrode in the hybrid electrolyte is also given in Fig. S4(a–c), which is reflected by the CV response (10–60 mV s^{-1}), GCD (2–5 A g^{-1}), and specific capacitance of $Ni(OH)_2$ nanoflowers at different current densities correspondingly.

To determine the kinetic parameters of the fabricated electrodes, EIS is also measured in the hybrid electrolyte. Fig. 8f represents the comparison of Nyquist plots of both the electrodes. It can be seen that the semi-circle of the NiO electrode is smaller than that of $Ni(OH)_2$ which exhibits a decrease in the charge transfer resistance (R_{ct}) at the electrode–electrolyte interface. The slope line in the low-frequency region is related to the Warburg impedance (Z_W) associated with the ion diffusion mechanism. An equivalent AC circuit model was used to evaluate the kinetic parameter, which was fitted using the *Z*-view software, as shown in the inset of Fig. 8f. The fitting parameters of R_{ct} and solution resistance R_s are presented in Table S1. The comparatively smaller R_{ct} value of the NiO electrode indicates the improved kinetics of the electrode. The enhanced performance of the NiO electrode is due to the fast ionic conductivity of Ni^{2+}/Ni^{3+} involved in the faradaic redox reaction, which is best for the charge storage capacity. The improved ionic transport in the hybrid electrolyte (KOH + Na_2SO_4) is due to the dual ionic species in the electrolyte, which produces synergistic effects and causes an easy ionic transport at the electrode–electrolyte interface. The KOH enhanced the redox properties while the Na_2SO_4 stabilized the electrode–electrolyte interface during the charge storage mechanism.[4] The faradaic behavior of the hybrid electrolyte boosts the

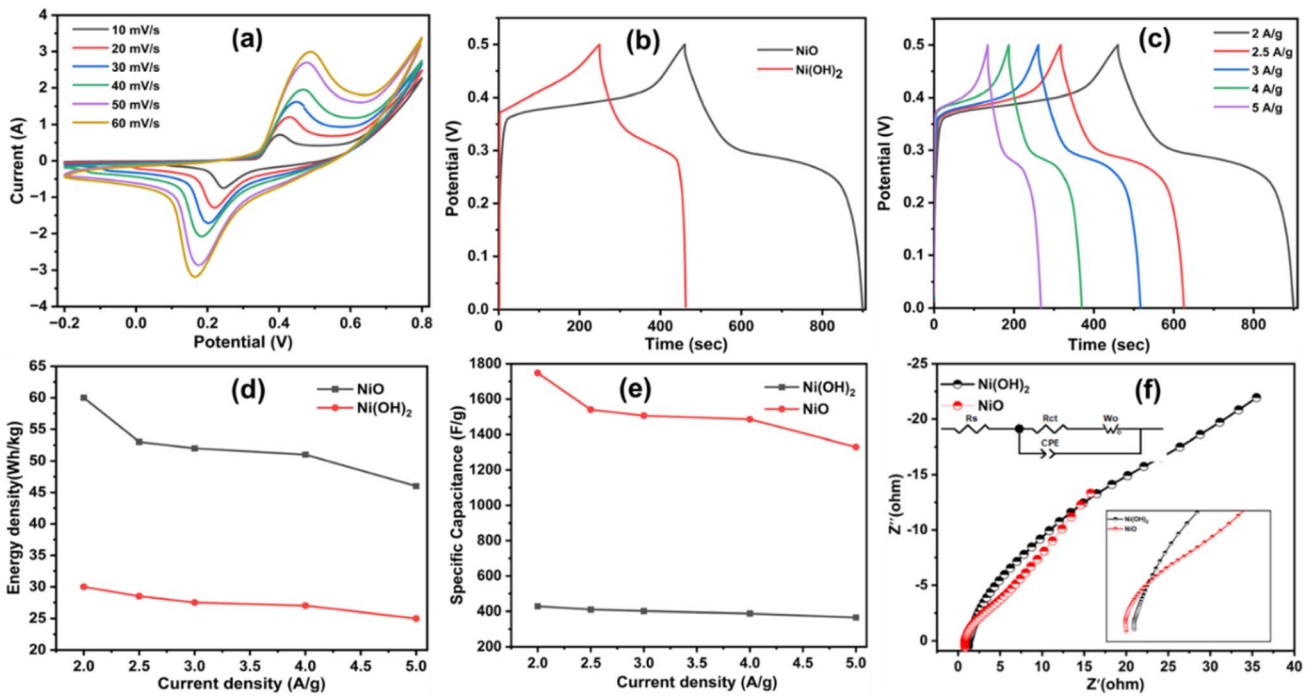

Fig. 8 Electrochemical performance of the NiO NPs in the hybrid electrolyte: (a) CV response of the NiO electrode in the hybrid electrolyte at different scan rates, (b) comparative analysis of the GCD curve of $Ni(OH)_2$ and NiO electrodes at 2 A g^{-1}, (c) GCD curves of the NiO electrode at different current densities, (d) current density *vs.* energy densities of $Ni(OH)_2$ and NiO, (e) specific capacitance of $Ni(OH)_2$ and NiO electrodes at different current densities, and (f) Nyquist plots of both the electrodes (inset shows the kinetic parameters of the electrodes).

Table 1 Comparison of the fabricated electrode with those reported in the literature

Material	Method	Specific capacitance (F g^{-1})	Electrolyte	References
NiO	Hydrothermal	132	1 M KOH	38
NiO NPs	Solvothermal	1386	1 M KOH	39
NiO	Sonochemical	449	1 M KOH	40
NiO NPs	Hydrothermal	1358	3 M KOH	41
NiO nanocrystal	Hydrothermal	200	1 M Na_2SO_4	42
NiO NPs	**Anodization**	**1748**	**Hybrid electrolyte**	**This work**

charge storage capacity of the NiO electrode. In the hybrid electrolyte, Na^+ and K^+ participate in redox reactions and their ionic sizes are 0.95 Å and 1.33 Å.[4] The small ionic sizes of Na^+ and K^+ contribute easily to the faradaic reaction during intercalation and de-intercalation between the electrode–electrolyte interfaces. The hybrid electrolyte maintains the charge storage mechanism by reducing the voltage fluctuations and improving the overall performance during charging and discharging phenomena.

3.5. Specific capacitance from CV in hybrid, KOH and Na_2SO_4 electrolytes

The specific capacitance *vs.* scan rate for all electrolytes, obtained from the CV curves, is presented in Fig. 9a. It can be seen that the hybrid electrolyte exhibits the highest specific capacitance of 1490 F g^{-1} at 0.01 V s^{-1}, followed by KOH (1011 F g^{-1}) and Na_2SO_4 (725 F g^{-1}) (Cs: hybrid > KOH > Na_2SO_4). The superior capacitance in the hybrid system is due to the synergistic effect of dual ionic species (K^+ and Na^+), which enhances charge storage at the electrode–electrolyte interface.

3.6. Charge storage mechanism in supercapacitors using *b*-values

To further clarify the charge-storage behavior, the relationship between the peak current density and scan rate is shown in Fig. 9(b–d). The slope value "*b*" from the log (*i*)–(*v*) plot demonstrates the charge storage mechanism, with the obtained

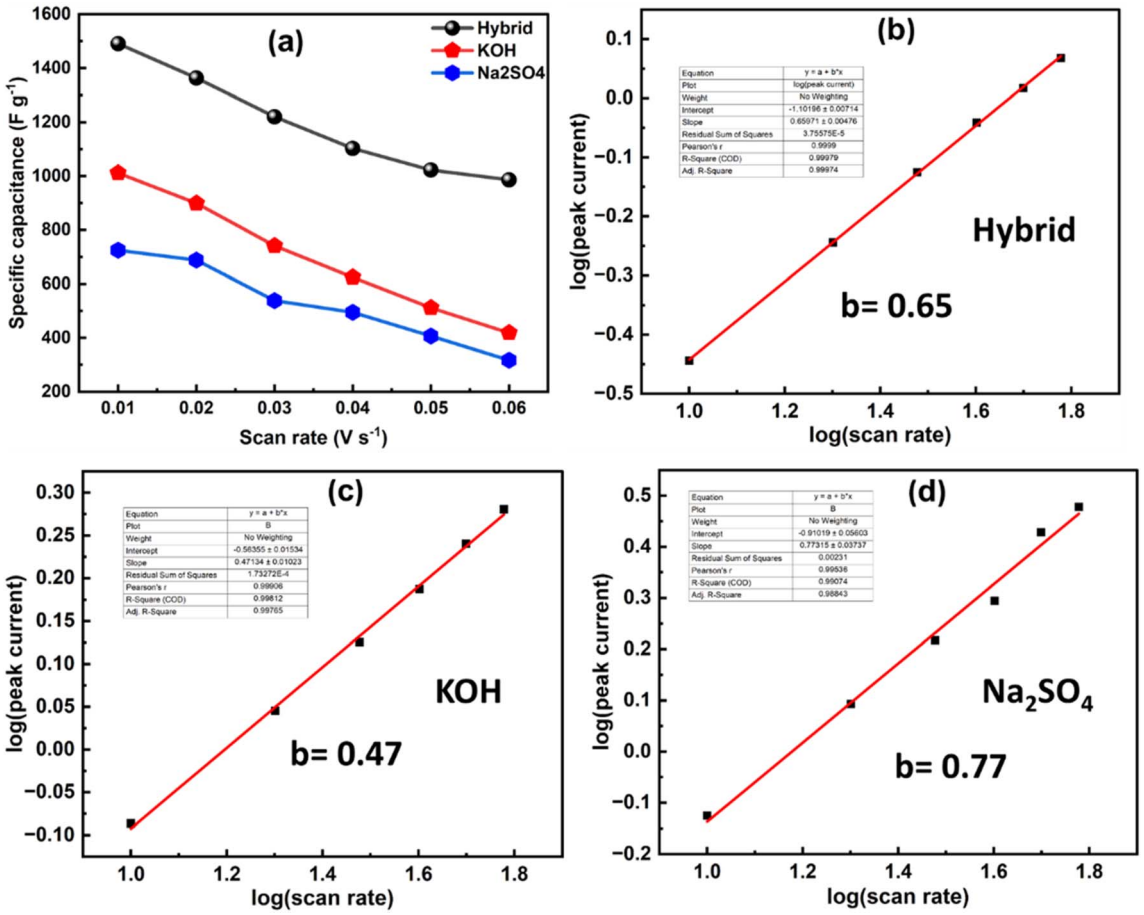

Fig. 9 (a) Graph of specific capacitance *vs.* scan rate in different electrolytes and (b–d) charge storage behavior in different electrolytes using *b*-values.

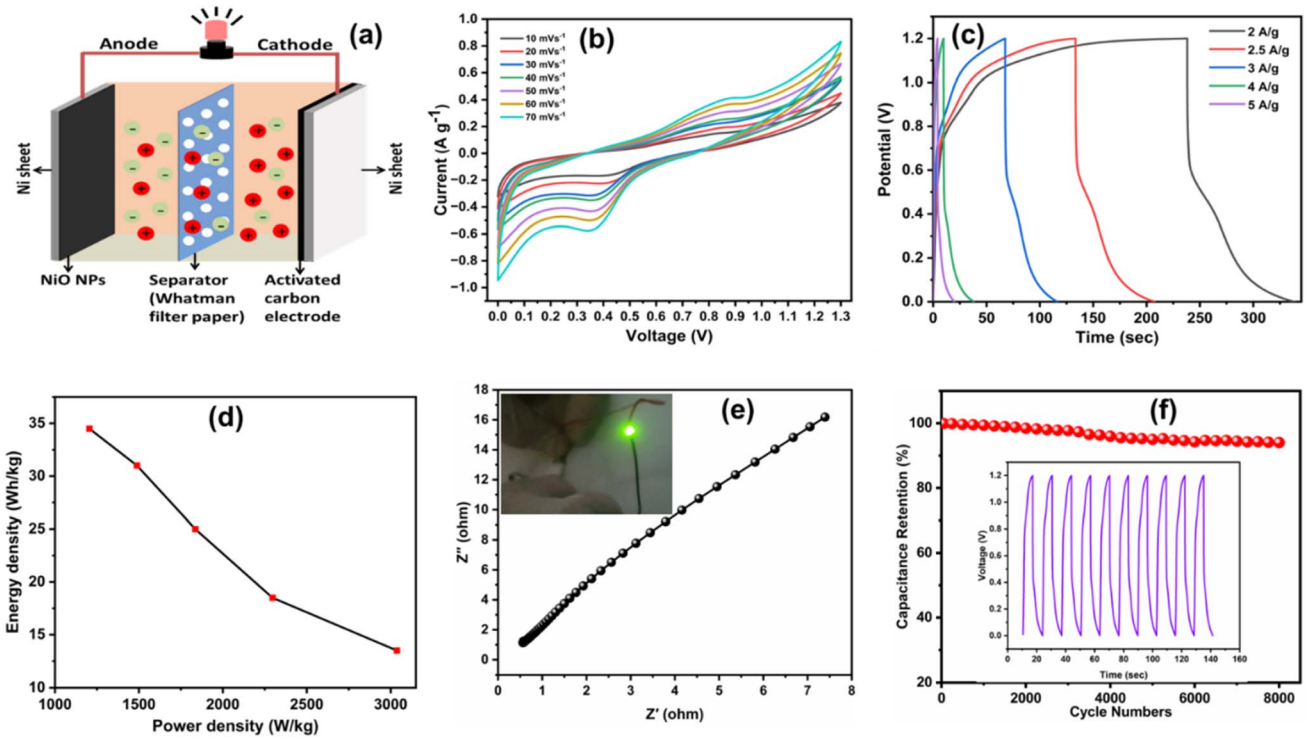

Fig. 10 Electrochemical performance of the NiO NPs//AC device: (a) schematic of the assembled NiO device, (b) CV response at different scan rates of the NiO//AC electrode, (c) GCD curve at different current densities, (d) Ragone plot of the fabricated device, (e) Nyquist plot of the device and inset show the LED, and (f) cycling stability of the NiO NPs//AC device (inset shows the charge–discharge for the first 10 cycles).

values of $b = 0.47$ (KOH), 0.77 (Na_2SO_4), and 0.65 (hybrid). The b-value close to 0.5 for KOH indicates a diffusion-controlled process, while the higher value (~0.77) for Na_2SO_4 suggests a predominantly surface-controlled redox process. The intermediate b-value ($0.5 < b < 1$) in the hybrid electrolyte (0.65) confirms the co-existence of both surface and diffusion-controlled charge-storage mechanism. Therefore, the presence of both surface and intercalation redox mechanisms in the hybrid electrolyte enhances the charge-storage capacity of the NiO electrode.

3.7. Electrochemical performance of the asymmetric supercapacitor ASC (NiO//AC) device

To evaluate the practical use of the NiO electrode, the SC device is assembled with NiO NPs as the positive electrode, activated carbon (AC) as the negative electrode, and separator in between the electrodes with the hybrid electrolyte. Fig. 10a depicts the schematic diagram of the internal mechanism that occurred inside the SC device. Fig. 10b displays the CV response of the ASC device measured at different scan rates (10 to 70 mVs^{-1}) in the potential window from 0 to 1.2 V in the hybrid electrolyte. It can be noted that at high scan rates, the CV retains its original shape, demonstrating the stability and excellent capacitive behavior of the fabricated device.[4] Moreover, the charge–discharge behavior can be seen from the GCD curve, in which the device achieved a maximum specific capacitance of 170 F g^{-1} at a current density of 1.5 A g^{-1} and maintained up to 87 F g^{-1} at 5 A g^{-1}, as shown in Fig. 10c. The specific capacitance of the ASC device with different current densities is given in Table S2. The Ragone plot of the ASC device is indicated in Fig. 10d. Interestingly, the device delivered a higher energy density (34.4 Wh kg^{-1}) in comparison with the previously reported NiO-based SC devices, such as NiO NPs (~25 Wh kg^{-1}),[33] honeycomb-like NiO (23.25 Wh kg^{-1}),[35] NiO/Ni-MOF-25 (31.3 Wh kg^{-1}),[36] and 1% Ce : NiO (26.27 Wh kg^{-1})[37] due to the synergistic effect of the hybrid electrolyte. Fig. 10e represents the Nyquist plot of the fabricated device, which demonstrates improved kinetic parameters, while the inset shows the glowing LED *via* our fabricated ASC device. The cyclic stability of any device is the most important consideration when investigating its practical application. Therefore, the charge–discharge cycle was repeated 8000 times at a current density of 5 A g^{-1}, with 94% capacitance retention (Fig. 10f). The inset shows cycling stability of the first 10 cycles.

4 Conclusion

In this study, $Ni(OH)_2$ nanoflowers were produced by the green anodization process, which were successfully transformed into NiO NPs *via* annealing and evaluated for supercapacitor applications. The electrochemical performance of NiO NPs was investigated using several aqueous electrolytic solutions such as KOH, Na_2SO_4, and their combination (hybrid). NiO NPs delivered an enhanced capacitance in the hybrid (1 M KOH: 1 M Na_2SO_4) electrolyte. The fabricated NiO NP-based electrode delivered a high capacitance of 1748 F g^{-1} at 2 A g^{-1} compared

to the $Ni(OH)_2$ nanoflower-based electrode, which is 428 F g^{-1}. The fabricated asymmetric device attains an energy density of 34.4 Wh kg^{-1} at a power density of 900 W kg^{-1}. Furthermore, the device maintains a capacitance retention of 94% after 8000 cycles. The significantly improved performance of NiO NPs is due to its high surface area, enhanced crystallinity, and the synergistic effect of the hybrid electrolyte.

Author contributions

G. A conceived the idea. M. D and J. A. designed the study and conducted the experiments. P. M and S. J. helped in the electrochemical studies. G. A, M. D., and J. A. analyzed the experimental data along with its interpretation. M. D and J. A. prepared the initial draft of the manuscript. M. H. B, A. S., R. G, A. F. K, and H. U helped in the characterizations and data analysis. N. K, M. K, Y. X, and I. S revised the initial draft and provided input for the improvement. G. A. funded the study and supervised the project. All the authors were involved in the discussion and writing of the manuscript. M. D., Y. X, and G. A. finalized the revised manuscript with inputs and comments from all the authors.

Conflicts of interest

The authors declare that they have no known competing financial interests or personal relationships that could have influenced the work reported in this study.

Data availability

The data supporting this article have been included in the main text of the manuscript as well as in the supplementary information (SI). Supplementary information: schematic of the anodization process, the overall mechanism from material synthesis to the electrochemical measurements of the electrodes, the FTIR spectra of $Ni(OH)_2$ and NiO, electrochemical measurements of the $Ni(OH)_2$ electrode in the hybrid electrolyte, kinetic parameters of $Ni(OH)_2$ and NiO electrodes, and the specific capacitance of the assembled device at different current densities. See DOI: https://doi.org/10.1039/d5ra07019h.

Acknowledgements

This work was financially supported by PINSTECH Phase-II.

References

1 S. Abbas, T. H. Bokhari, A. Zafar, S. Javed, S. Karim, H. Sun, S. Hussain, A. Khalid, Y. Yu, R. T. A. Khan, I. Ullah, A. Nisar and M. Ahmad, Zn Doping Induces Rich Oxygen Vacancies in δ-MnO2 Flower-like Nanostructures for Impressive Energy Density Coin Cell Supercapacitor, *J. Energy Storage*, 2024, **87**, 111455, DOI: 10.1016/j.est.2024.111455.

2 J. Wu, W. Raza, P. Wang, A. Hussain, Y. Ding, J. Yu, Y. Wu and J. Zhao, Zn-Doped MnO2 Ultrathin Nanosheets with Rich Defects for High Performance Aqueous Supercapacitors, *Electrochim. Acta*, 2022, **418**, 140339, DOI: 10.1016/j.electacta.2022.140339.

3 Design and Mechanisms of Asymmetric Supercapacitors | Chemical Reviews, https://pubs.acs.org/doi/full/10.1021/acs.chemrev.8b00252?casa_token=H6MvyjZtoBoAAAAA%3A_wHShl6MG_OYJhEy-d4Ad4ZMF8CtQN7JcZsNqkXug-5PZo0Ua8PzGUjX6zUKl6FGsI9LOd7s8FbTcF3, accessed 2025-04-20.

4 S. Abbas, T. H. Bokhari, M. Abbas, Z. Abbas, A. Khalid, S. Javed, A. Zafar, N. Ahmad, S. Karim, A. Javed, T. Zhu, A. Nisar and M. Ahmad, High Performance α-Fe2O3/rGO Based Prototype Asymmetric Coin Cell Supercapacitor in Hybrid Electrolyte, *Electrochim. Acta*, 2025, **517**, 145761, DOI: 10.1016/j.electacta.2025.145761.

5 X. Wu and S. Yao, Flexible Electrode Materials Based on WO3 Nanotube Bundles for High Performance Energy Storage Devices, *Nano Energy*, 2017, **42**, 143–150, DOI: 10.1016/j.nanoen.2017.10.058.

6 M. Liu, Z. Qin, X. Yang, Z. Lin and T. Guo, Fabricating Controllable Hierarchical Pores on Smooth Carbon Sheet for Synthesis of Supercapacitor Materials, *Vacuum*, 2019, **168**, 108806, DOI: 10.1016/j.vacuum.2019.108806.

7 J. Mu, J. Wang, J. Hao, P. Cao, S. Zhao, W. Zeng, B. Miao and S. Xu, Hydrothermal Synthesis and Electrochemical Properties of V2O5 Nanomaterials with Different Dimensions, *Ceram. Int.*, 2015, **41**(10, Part A), 12626–12632, DOI: 10.1016/j.ceramint.2015.06.091.

8 J. Wang, W. Li, Y. Ge, J. Shen, Y. Zhao, Y. Zhang and J. Yuan, Design and Synthesis of Porous TiO2@C Nanotube Bundles with Enhanced Supercapacitive Performance, *Ceram. Int.*, 2017, **43**(2), 2876–2880, DOI: 10.1016/j.ceramint.2016.11.045.

9 U. K. Chime, A. C. Nkele, S. Ezugwu, A. C. Nwanya, N. M. Shinde, M. Kebede, P. M. Ejikeme, M. Maaza and F. I. Ezema, Recent Progress in Nickel Oxide-Based Electrodes for High-Performance Supercapacitors, *Curr. Opin. Electrochem.*, 2020, **21**, 175–181, DOI: 10.1016/j.coelec.2020.02.004.

10 M. Mustaqeem, G. A. Naikoo, F. Rahimi, M. Z. Pedram, H. Pourfarzad, I. U. Hassan, F. Arshad and Y.-F. Chen, Rational Design of Cu Based Composite Electrode Materials for High-Performance Supercapacitors – A Review, *J. Energy Storage*, 2022, **51**, 104330, DOI: 10.1016/j.est.2022.104330.

11 K. John Steven Wesley, K. Shireesha, V. Divya, D. Rakesh, C. H. Shilpa Chakra, K. Sree Chandana, S. Sai Vamsi Ganesh Reddy, K. Deepti, T. Bala Narsaiah and K. Sadhana, Impact of Surfactant on Specific Capacitance of Nickel Oxide Nanoparticles for Supercapacitor Application, *Bull. Mater. Sci.*, 2024, **47**(1), 30, DOI: 10.1007/s12034-023-03101-3.

12 W. Deng, Y. Liu, Y. Zhang, F. Lu, Q. Chen and X. Ji, Enhanced Electrochemical Capacitance of Nanoporous NiO Based on an Eggshell Membrane, *RSC Adv.*, 2012, **2**(5), 1743, DOI: 10.1039/c2ra00885h.

13 A. A. Yadav, Y. M. Hunge and S. B. Kulkarni, Synthesis of Multifunctional FeCo2O4 Electrode Using Ultrasonic

Treatment for Photocatalysis and Energy Storage Applications, *Ultrason. Sonochem.*, 2019, **58**, 104663, DOI: 10.1016/j.ultsonch.2019.104663.

14 A. A. Yadav, Y. M. Hunge and S. B. Kulkarni, Chemical Synthesis of Co3O4 Nanowires for Symmetric Supercapacitor Device, *J. Mater. Sci. Mater. Electron.*, 2018, **29**(19), 16401–16409, DOI: 10.1007/s10854-018-9731-7.

15 M. Salavati-Niasari, F. Davar and Z. Fereshteh, Synthesis of Nickel and Nickel Oxide Nanoparticles via Heat-Treatment of Simple Octanoate Precursor, *J. Alloys Compd.*, 2010, **494**(1), 410–414, DOI: 10.1016/j.jallcom.2010.01.063.

16 M. N. rifaya, T. Theivasanthi and M. Alagar, Chemical Capping Synthesis of Nickel Oxide Nanoparticles and Their Characterizations Studies, *Nanosci. Nanotechnol.*, 2012, **2**(5), 134–138, DOI: 10.5923/j.nn.20120205.01.

17 A. S. Danial, M. M. Saleh, S. A. Salih and M. I. Awad, On the Synthesis of Nickel Oxide Nanoparticles by Sol–Gel Technique and Its Electrocatalytic Oxidation of Glucose, *J. Power Sources*, 2015, **293**, 101–108, DOI: 10.1016/j.jpowsour.2015.05.024.

18 G. Ali, Y. J. Park, J. W. Kim and S. O. Cho, A Green, General, and Ultrafast Route for the Synthesis of Diverse Metal Oxide Nanoparticles with Controllable Sizes and Enhanced Catalytic Activity, *ACS Appl. Nano Mater.*, 2018, **1**(11), 6112–6122, DOI: 10.1021/acsanm.8b01220.

19 J. Zhao, H. Liu and Q. Zhang, Preparation of NiO Nanoflakes under Different Calcination Temperatures and Their Supercapacitive and Optical Properties, *Appl. Surf. Sci.*, 2017, **392**, 1097–1106, DOI: 10.1016/j.apsusc.2016.09.128.

20 A novel route to the formation of 3D nanoflower-like hierarchical iron oxide nanostructure - IOPscience. https://iopscience.iop.org/article/10.1088/1361-6528/aaf52a/meta, accessed 2025-07-31.

21 H. Ullah, R. Ahmad, A. A. Khan, N. Khaliq, M. Khan, G. Ali, S. Karim, X. Yi and S. O. Cho, A Sensitive Non-Enzymatic Glucose Sensor Based on MgO Entangled Nanosheets Decorated with CdS Nanoparticles: Experimental and DFT Study, *J. Mol. Liq.*, 2022, **360**, 119366, DOI: 10.1016/j.molliq.2022.119366.

22 Fabrication of High-Performance Asymmetric Supercapacitor Consists of Nickel Oxide and Activated Carbon (NiO//AC). https://www.mdpi.com/2073-4344/12/4/375, accessed 2025-07-06.

23 Z. Abbas, T. Hussain Bokhari, Z. Rana, S. Ijaz, E. Gul, A. Zafar, S. Javaid, M. Gul, K. Maaz, S. Karim, G. Xiang, M. Ahmad and A. Nisar, Mesoporous Mo-Doped $NiCo_2O_4$ Nanocrystals for Enhanced Electrochemical Kinetics in High-Performance Lithium-Ion Batteries, *RSC Adv.*, 2025, **15**(17), 13552–13560, DOI: 10.1039/D5RA00918A.

24 Q. Xu, Y. Zhu, Q. Han, R. Zhao, Y. Zhuang, Y. Liu, S. Zhang and C. Miao, Preparation of Yb-Substituted α-Ni(OH)2 and Its Physicochemical Properties, *J. Alloys Compd.*, 2014, **584**, 1–6, DOI: 10.1016/j.jallcom.2013.08.097.

25 X. Yi, V. Celorrio, H. Zhang, N. Robertson and C. Kirk, α/β-Ni(OH) 2 Phase Control by F-Ion Incorporation to Optimise Hybrid Supercapacitor Performance, *J. Mater. Chem. A*, 2023, **11**(41), 22275–22287, DOI: 10.1039/D3TA04731H.

26 I. Shakir, Z. Almutairi, S. S. Shar and A. Nafady, Nickel Hydroxide Nanoparticles and Their Hybrids with Carbon Nanotubes for Electrochemical Energy Storage Applications, *Results Phys.*, 2020, **17**, 103117, DOI: 10.1016/j.rinp.2020.103117.

27 N. Duraisamy, K. Kandiah, R. Rajendran, P. S, R. R and G. Dhanaraj, Electrochemical and Photocatalytic Investigation of Nickel Oxide for Energy Storage and Wastewater Treatment, *Res. Chem. Intermed.*, 2018, **44**(9), 5653–5667, DOI: 10.1007/s11164-018-3446-5.

28 L. Aguilera, Y. Leyet, A. Almeida, J. A. Moreira, J. P. De La Cruz, E. A. Milán-Garcés, R. R. Passos and L. A. Pocrifka, Electrochemical Preparation of Ni(OH)2/CoOOH Bilayer Films for Application in Energy Storage Devices, *J. Alloys Compd.*, 2021, **874**, 159858, DOI: 10.1016/j.jallcom.2021.159858.

29 A. Sunny and K. Balasubramanian, Laser-induced Phonon and Magnon Properties of NiO Nanoparticles: A Raman Study, *J. Raman Spectrosc.*, 2021, **52**(4), 833–842, DOI: 10.1002/jrs.6067.

30 E. Aytan, B. Debnath, F. Kargar, Y. Barlas, M. M. Lacerda, J. X. Li, R. K. Lake, J. Shi and A. A. Balandin, Spin - Phonon Coupling in Nickel Oxide Determined from Ultraviolet Raman Spectroscopy, *Appl. Phys. Lett.*, 2017, **111**(25), 252402, DOI: 10.1063/1.5009598.

31 A. Sunny and K. Balasubramanian, Plasmon Induced Enhancement of Surface Optical Phonon Modes and Magnon Properties of NiO Nanoparticles: Raman Spectral Probe, *Phys. Chem. Chem. Phys.*, 2020, **22**(39), 22815–22822, DOI: 10.1039/D0CP03720F.

32 Y. Cheng, M. Guo, M. Zhai, Y. Yu and J. Hu, Nickel Nanoparticles Anchored onto Ni Foam for Supercapacitors with High Specific Capacitance, *J. Nanosci. Nanotechnol.*, 2020, **20**(4), 2402–2407, DOI: 10.1166/jnn.2020.17377.

33 S. S. Gunasekaran, A. Gopalakrishnan, R. Subashchandrabose and S. Badhulika, Phytogenic Generation of NiO Nanoparticles as Green-Electrode Material for High Performance Asymmetric Supercapacitor Applications, *J. Energy Storage*, 2021, **37**, 102412, DOI: 10.1016/j.est.2021.102412.

34 G. Cai, X. Wang, M. Cui, P. Darmawan, J. Wang, A. L.-S. Eh and P. S. Lee, Electrochromo-Supercapacitor Based on Direct Growth of NiO Nanoparticles, *Nano Energy*, 2015, **12**, 258–267, DOI: 10.1016/j.nanoen.2014.12.031.

35 X. Ren, C. Guo, L. Xu, T. Li, L. Hou and Y. Wei, Facile Synthesis of Hierarchical Mesoporous Honeycomb-like NiO for Aqueous Asymmetric Supercapacitors, *ACS Appl. Mater. Interfaces*, 2015, **7**(36), 19930–19940, DOI: 10.1021/acsami.5b04094.

36 G. Wang, Z. Yan, N. Wang, M. Xiang and Z. Xu, NiO/Ni Metal–Organic Framework Nanostructures for Asymmetric Supercapacitors, *ACS Appl. Nano Mater.*, 2021, **4**(9), 9034–9043, DOI: 10.1021/acsanm.1c01628.

37 S. R. Gawali, D. P. Dubal, V. G. Deonikar, S. S. Patil, S. D. Patil, P. Gomez-Romero, D. R. Patil and J. Pant, Asymmetric Supercapacitor Based on Nanostructured Ce-Doped NiO (Ce:NiO) as Positive and Reduced Graphene

Oxide (rGO) as Negative Electrode, *ChemistrySelect*, 2016, **1**(13), 3471–3478, DOI: **10.1002/slct.201600566**.

38 S. D. Dhas, P. S. Maldar, M. D. Patil, A. B. Nagare, M. R. Waikar, R. G. Sonkawade and A. V. Moholkar, Synthesis of NiO Nanoparticles for Supercapacitor Application as an Efficient Electrode Material, *Vacuum*, 2020, **181**, 109646, DOI: **10.1016/j.vacuum.2020.109646**.

39 G. Cai, X. Wang, M. Cui, P. Darmawan, J. Wang, A. L.-S. Eh and P. S. Lee, Electrochromo-Supercapacitor Based on Direct Growth of NiO Nanoparticles, *Nano Energy*, 2015, **12**, 258–267, DOI: **10.1016/j.nanoen.2014.12.031**.

40 N. Duraisamy, A. Numan, S. O. Fatin, K. Ramesh and S. Ramesh, Facile Sonochemical Synthesis of Nanostructured NiO with Different Particle Sizes and Its Electrochemical Properties for Supercapacitor Application, *J. Colloid Interface Sci.*, 2016, **471**, 136–144, DOI: **10.1016/j.jcis.2016.03.013**.

41 G. Manibalan, G. Murugadoss, P. Kuppusami, N. Kandhasamy and M. Rajesh Kumar, Synthesis of Heterogeneous NiO Nanoparticles for High-Performance Electrochemical Supercapacitor Application, *J. Mater. Sci. Mater. Electron.*, 2021, **32**(5), 5945–5954, DOI: **10.1007/s10854-021-05315-9**.

42 M. Jayachandran, S. Kishore babu, T. Maiyalagan, M. R. Kannan, R. Goutham kumar, Y. Sheeba Sherlin and T. Vijayakumar, Effect of Various Aqueous Electrolytes on the Electrochemical Performance of Porous NiO Nanocrystals as Electrode Material for Supercapacitor Applications, *Mater. Lett.*, 2021, **302**, 130415, DOI: **10.1016/j.matlet.2021.130415**.